

# On the importance of horizontal components in source-encoded elastic full-waveform inversion: Multicomponent ocean-bottom-node data

Armando Espindola-Carmona<sup>1</sup>, Jürgen Hoffmann<sup>2</sup>, Frederik J. Simons<sup>1</sup>, and Jeroen Tromp<sup>1,3</sup>

<https://doi.org/10.1190/tle44050154.1>

## Abstract

Elastic full-waveform inversion (EFWI) is a state-of-the-art seismic tomographic method. Recent advances in technology and instrumentation, combining crosstalk-free source-encoded FWI (SE-FWI) with multicomponent marine data acquisition using ocean-bottom nodes (OBNs), enable full-physics wave propagation and parameter inversion without the computational burden of traditional FWI. With OBN acquisition, P waves, S waves, and P-to-S conversions are recorded. It is not well understood to what extent adding horizontal components to SE-FWI improves the resolution of subsurface modeling. We assess their potential for the reconstruction of shear and compressional wave speeds ( $V_p$  and  $V_s$ ) by using a synthetic data set modeled after a recently acquired OBN survey in the North Sea. We perform synthetic inversion tests to design suitable strategies that leverage the information recorded in the horizontal components of the data to improve the reconstructed model resolution laterally and in depth. We advocate for a hierarchical inversion approach to recover the elastic parameters. We exploit the P and P-to-S converted waves recorded on the horizontal components to robustly reconstruct both  $V_p$  and  $V_s$ . Adding horizontal components to the SE-FWI modeling workflow results in improved spatial resolution, enhanced depth coverage, and more accurate elastic wave speed estimates.

## Introduction

Full-waveform inversion (FWI) is a method used to obtain high-resolution descriptions of the physical properties of the subsurface. Introduced by Lailly and Bednar (1983) and Tarantola (1984), FWI seeks to minimize the differences between synthetic and observed data by using an adjoint-state formalism (Tromp et al., 2005; Plessix, 2006). Although FWI has been successfully applied at the exploration, regional, and global scales, the technique is still computationally expensive, scaling linearly with the number of seismic sources in the data set. Source “encoding” alleviates this issue by combining multiple sources in a single super simulation. Naive approaches introduce crosstalk between the sources, which is detrimental to the quality of the images (Romero et al., 2000; Krebs et al., 2009). Recent source-encoding strategies, developed for the discrete-time Fourier domain, become crosstalk-free after the wavefield reaches steady state (Schuster et al., 2011;

Zhang et al., 2018; Tromp and Bachmann, 2019). Because source-encoded FWI (SE-FWI) in the spectral domain complicates time windowing to isolate specific seismic arrivals, Liu et al. (2024) proposed a Laplace-domain source-encoding strategy that dampens specific arrivals at a specific rate, gradually feeding later arrivals into the inversion.

Ocean-bottom nodes (OBNs) have become the high-end acquisition method in marine seismic exploration. Compared to classic streamer surveys, OBNs can record high-quality four-component data (pressure and particle velocity) at longer offsets and over wider azimuths (Zhang et al., 2021). Despite these advantages, it is still common practice in FWI to only use the pressure and the vertical particle motion of the seismic wavefield (Solano and Plessix, 2023). Such data restriction is often used to justify using the acoustic approximation to reduce nonlinearity and computational cost (Pratt, 1999; Operto et al., 2015). However, more realistic descriptions of the physical properties of the subsurface are needed, particularly due to the rising complexity of reservoir targets. In this study, we apply elastic SE-FWI in a marine environment using a multicomponent OBN synthetic data set (see also Cho et al. [2022]), mimicking a realistic OBN survey in the North Sea. We perform different synthetic inversion tests to design suitable strategies to leverage the information recorded in the horizontal components of the data (in particular, S waves and P-to-S conversions) and to improve the reconstructed model resolution laterally and in depth. We qualitatively and quantitatively analyze the resolution improvement of the elastic model parameters.

## Methodology

In this section, we briefly summarize the theory behind SE-FWI and discuss our inversion workflow.

**Source encoding in the Fourier domain.** With SE-FWI, we aim to find a model  $\mathbf{m}$  that minimizes the difference between the Fourier coefficients of observed data and synthetics, using a suitable metric to reduce cycle skipping and other nonlinearities of the inverse problem. Following Tromp and Bachmann (2019) and Bachmann and Tromp (2020), a certain data functional  $\Phi[s_i^o(\mathbf{x}, \omega; \mathbf{m}), d_i^s(\mathbf{x}, \omega)]$  measures the difference between Fourier coefficients at a single frequency  $\omega$ , of observed  $d_i^s(\mathbf{x}, \omega)$  and simulated data  $s_i^o(\mathbf{x}, \omega; \mathbf{m})$  on the  $i^{\text{th}}$  of  $N_c$  components, counting

Manuscript received 14 December 2024; accepted 10 February 2025.

<sup>1</sup>Princeton University, Department of Geosciences, Princeton, New Jersey, USA. E-mail: ae2415@princeton.edu; fjsimons@alum.mit.edu; jtromp@princeton.edu.

<sup>2</sup>DNO ASA, Oslo, Norway. E-mail: jurgen.hoffmann@dno.no.

<sup>3</sup>Princeton University, Department of Applied and Computational Mathematics, Princeton, New Jersey, USA.

$s = 1, \dots, S$  sources and  $r = 1, \dots, R$  receivers. The misfit functional sums over sources, receivers, and components:

$$\chi = \frac{1}{2} \sum_{s=1}^S \sum_{r=1}^R \Phi [s_i^s(\mathbf{x}_r, \omega; \mathbf{m}), d_i^s(\mathbf{x}_r, \omega)]. \quad (1)$$

We follow different workflows to process data and synthetics. We Fourier transform the observed data  $d_i^s(\mathbf{x}_r, t)$  for all labeled sources  $s$ , receivers  $r$ , and components  $i$ :

$$d_i^s(\mathbf{x}_r, \omega) = \int_0^T d_i^s(\mathbf{x}_r, t) e^{-i\omega t} dt, \quad (2)$$

where  $T$  is any time greater than the time  $T_{ss}$  after which the Fourier or Laplace coefficients reach steady state. In general, we take the largest  $T_{ss}$  across the data set. To compute the synthetic data and extract their Fourier coefficients, we use a superposition of monochromatic sources with a frequency  $\omega_s$ . These sources are combined into a super forward simulation of a seismic wavefield  $s_i^s(\mathbf{x}_r, t; \mathbf{m})$  that reaches steady state after  $T_{ss}$ . The orthogonality of the Fourier basis functions over the finite duration:

$$\Delta\tau = \frac{2\pi}{\Delta\omega} = \frac{2\pi(S)}{\omega_{max} - \omega_{min}}, \quad (3)$$

defined by the number of encoding sources  $S$  and the bandwidth  $[\omega_{min}, \omega_{max}]$ , and ensures extraction of the individual Fourier coefficients over the time interval  $[T_{ss}, T_{ss} + \Delta\tau]$ :

$$s_i^s(\mathbf{x}_r, \omega_s; \mathbf{m}) = \frac{2}{\Delta\omega} \int_{T_{ss}}^{T_{ss} + \Delta\tau} s_i^s(\mathbf{x}_r, t; \mathbf{m}) e^{-i\omega_s t} dt. \quad (4)$$

Here,  $\omega_s = \omega_{min} + (s - 1)\Delta\omega$  is evenly spaced and uniquely assigned to each source  $s$  in the super forward simulation. With those, we compute the adjoint source-time function for the chosen measure  $\Phi$ , and hence the variation of the misfit functional  $\chi$  with respect to the model parameters  $\frac{\partial\chi}{\partial\mathbf{m}}$ . The combination of super forward and super adjoint simulations, at randomized frequencies as the iterations progress, ultimately incorporates information from all sources and stations in the data set over the entire bandwidth. The time to reach steady state  $T_{ss}$  depends on the spatial dimension of the domain and the seismic wavespeeds within it (Bachmann and Tromp, 2020; Cui et al., 2023). We determine the steady-state time of the simulation by running a super forward simulation and monitoring the seismic energy of the wavefield. We assume that the simulation has reached steady state when the energy of the seismic wavefield has reduced by five orders of magnitude.

**Source encoding in the Laplace domain.** Although Fourier-domain SE-FWI has been applied successfully in medical imaging and seismic exploration (Bachmann and Tromp, 2020; Liu et al., 2024), two drawbacks arise. First, time-domain windowing for data selection is impossible in the frequency domain, and care must be taken not to violate Fourier orthogonality. Second, reaching steady state may be challenging due to the size of the simulation

domain, source and station geometry, or the recorded duration of the observed data.

These issues can be alleviated by switching to the Laplace domain. Source encoding for FWI in the Laplace domain is described in detail by Liu et al. (2024) and briefly summarized here. The Laplace coefficients for observed  $d_i^s(\mathbf{x}_r, z_s)$  and synthetic data  $s_i^s(\mathbf{x}_r, z_s)$  are computed similarly to equations 2 and 4, that is,

$$d_i^s(\mathbf{x}_r, z_s) = e^{\gamma t_0} \int_0^T d_i^s(\mathbf{x}_r, t) e^{-z t} dt, \quad (5)$$

$$s_i^s(\mathbf{x}_r, z_s; \mathbf{m}) = e^{\gamma t_0} \frac{2}{\Delta\tau} \int_{T_{ss}}^{T_{ss} + \Delta\tau} s_i^s(\mathbf{x}_r, t; \mathbf{m}) e^{-z t} dt. \quad (6)$$

Here,  $z_s = \gamma + i\omega_s$  is the complex argument, and  $\gamma$  and  $\omega_s$  are real-valued. The Laplace coefficients induce an exponential damping function  $e^{-\gamma(t-t_0)}$ , and  $\gamma$  is adjusted throughout the inversion, typically focusing on early arrivals before gradually decreasing to include later phases, in multiscale inversion fashion (Bunks et al., 1995; Shin and Cha, 2009). Additionally, the damping factor  $\gamma$  reduces the time to reach steady state, decreasing the computational time of both forward and adjoint super simulations. The times  $t_0^{si}$  can be selected for each source-receiver pair to keep specific seismic wave types (e.g., converted waves, free-surface reflections, or surface waves) in order to reduce the nonlinearity of the inverse problem.

## SE-FWI inversion workflow

Our inversion workflow is divided into the following steps:

- 1) Initial model building
- 2) Data preprocessing (Laplace coefficients at randomized frequencies)
- 3) Forward (super) simulation and adjoint-source computation
- 4) Adjoint (super) simulation and gradient computation
- 5) Postprocessing (regularization and model update)

Steps 2–5 are performed iteratively to minimize the misfit function.

**Target model.** To perform the numerical examples, we use a realistic model from the North Sea (Figure 1). The model is 16 km long and 6 km deep, and seafloor depth is approximately 400 m. Because the model was initially defined in terms of compressional wave speed ( $V_p$ ), we employ an empirical relation to build shear wave speed ( $V_s$ ) and density ( $\rho$ ) models (Gardner et al., 1974; Castagna et al., 1985). The empirical rules were approximated by borehole data in the region of study  $V_s = 0.7263V_p - 728$  and  $\rho = 0.33V_p 0.2525$ . There are two main target formations. The first is associated with interlayered sandstones and claystones at a depth of about 4000 m. This formation contains water, gas, and oil. The second formation is located at about 4225 m depth, saturated with gas and water. To simulate these geologic formations in our target model, we add  $V_p$  and  $V_s$  relative perturbations of  $\pm 10\%$  and  $\pm 25\%$  respectively, with respect to the background model. In Figure 2, we show a common receiver gather from the target model (horizontal and vertical components). We observe the direct P-wave arrival, P-to-S conversions at the seafloor, and more complex events (reflections and refractions).

**Initial model.** The initial wave speed models are built by smoothing the true models with a 2D Gaussian function, with

vertical and horizontal standard deviation of about 250 m, resulting in a wavelength resolution of about 500 m (Figure 1). The water layer is considered to be known, to reduce any error in the fluid/solid boundary condition, important for seismic amplitudes. To compare the initial and target models, we extract logs from the models at 10 km horizontal distance (Figure 3).

**Data preprocessing.** We consider a multicomponent marine data acquisition using OBNs with a maximum offset of 13 km, 10 OBNs spaced 1 km, and 150 sources spaced 150 m. The depth of the pressure source is 10 m below the sea surface. The target data are simulated by a Ricker source wavelet with a dominant frequency of 5 Hz. The frequency range of the simulations lies between 2 and 9 Hz, and the record length for each shot is 10 s.

We transform the observed data to the Laplace domain, selecting a variable damping parameter  $\gamma$  through the inversion, and  $t_0^{sj}$  given by the first-break time for each source-receiver pair, computed using an average velocity and the distance from the source to the receivers.

**Forward simulation.** To compute the synthetic Laplace coefficients, we run a super forward simulation, in which we encode a randomly selected subset of sources. Each source is assigned to a specific frequency  $\omega_s$ , within the available band in the frequency range of the inversion, following a sinusoidal time function with amplitude increasing exponentially according to the (un-) damping parameter  $\gamma$ .

Because the number of OBNs is smaller than the number of sources, we use reciprocity to further reduce the computational cost. The duration of the simulation is the time to reach steady state  $T_{ss}$  plus the decoding time  $\Delta\tau$ , which depends on the

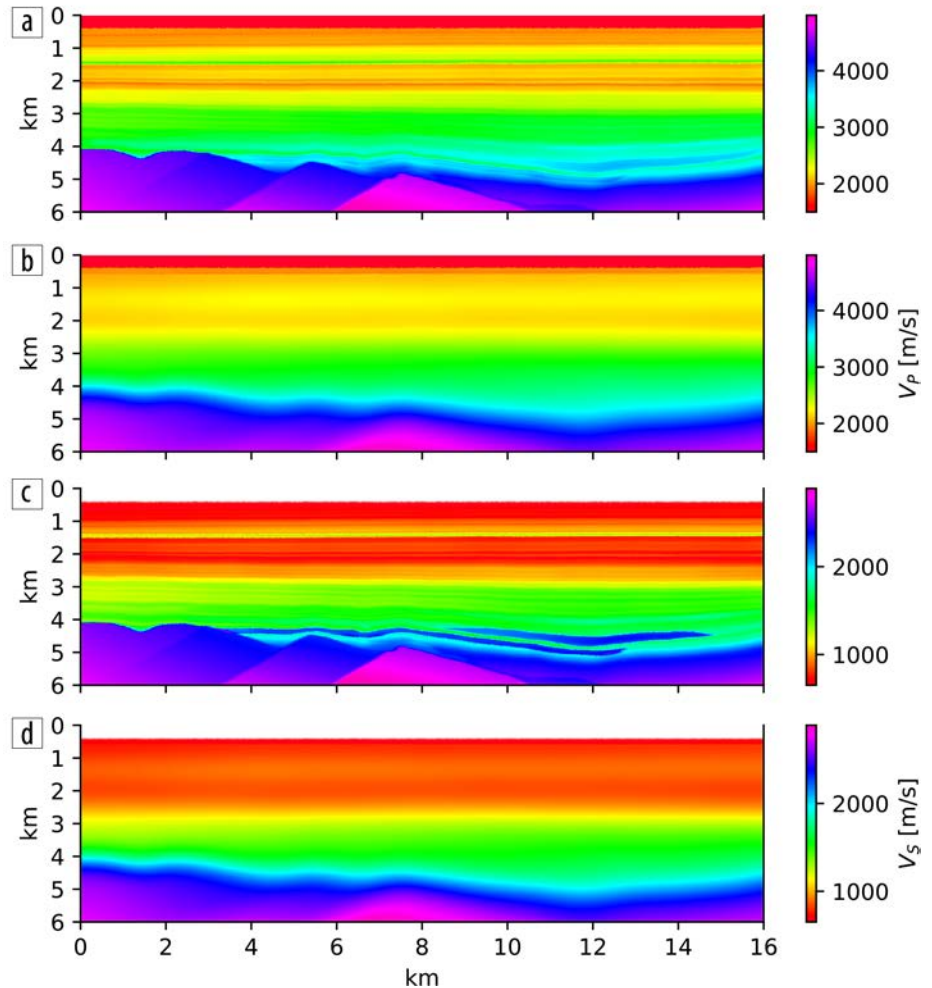


Figure 1. (a)  $V_p$  target model. (b)  $V_p$  initial model. (c)  $V_s$  target model. (d)  $V_s$  initial model.

Table 1. Inversion stages for vertical component inversion.

Stage	Data type	Inversion parameters	Misfit	Damping	Iteration numbers	Offset $t_0^{sj}$	Frequency Band
S1	Z	$V_p$	$\chi_\theta$	$1.1 \text{ s}^{-1}$	250	3 s	2–5 Hz
S2	Z	$V_p, V_s$	$\chi_\theta$	$0.6 \text{ s}^{-1}$	100	4 s	2–5 Hz
S3	Z	$V_p, V_s$	$\chi_\theta$	$0.6 \text{ s}^{-1}$	100	5 s	2–9 Hz
S4	Z	$V_p, V_s$	$\chi_\theta$	$0.3 \text{ s}^{-1}$	300	5 s	2–9 Hz

Table 2. [Caption needed].

Stage	Data type	Inversion parameters	Misfit	Damping	Iteration numbers	Offset $t_0^{sj}$	Frequency Band
S1	Z	$V_p$	$\chi_\theta$	$1.1 \text{ s}^{-1}$	250	3 s	2–5 Hz
S2	Z	$V_p, V_s$	$\chi_\theta$	$0.6 \text{ s}^{-1}$	100	4 s	2–5 Hz
S3	X,Z	$V_p, V_s$	$\chi_\theta$	$0.6 \text{ s}^{-1}$	100	5 s	2–9 Hz
S4	X,Z	$V_p, V_s$	$\chi_\theta$	$0.3 \text{ s}^{-1}$	300	5 s	2–9 Hz

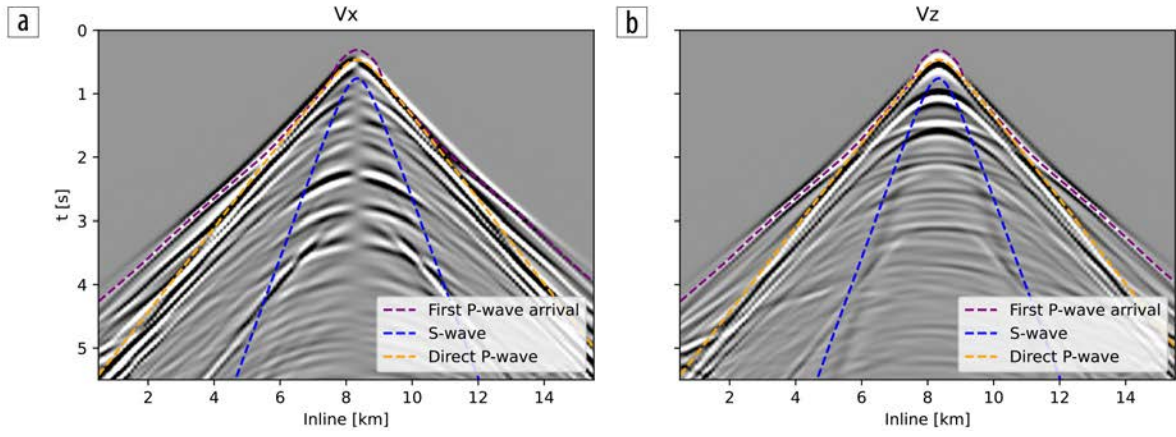


Figure 2. (a) Horizontal and (b) vertical common receiver gather of the target data.

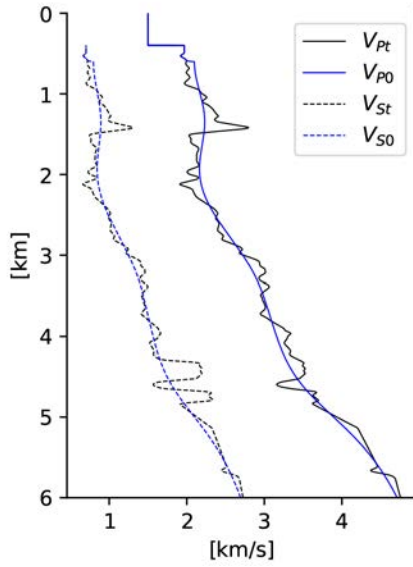


Figure 3. Vertical profiles at 10 km inline distance.  $V_p$  target (black line) and initial model (blue line).  $V_s$  target (black dashed line) and initial model (blue dashed line).

frequency band and the number of sources (equation 3). In all the numerical experiments, we keep the same steady-state time  $T_{ss} = 10$  s and decoding time  $\Delta\tau = 20$  s. These specific parameters allow us to encode 140 sources simultaneously. For all simulations, we apply absorbing and free-surface boundary conditions around the domain and at the top, respectively.

**Adjoint simulation.** FWI is an ill-posed inverse problem, hence multiple models may fit the data, and its nonlinear nature requires a reliable starting model and a suitable metric to compare the observed and synthetic data to prevent cycle skipping and avoid getting stuck in local minima. To alleviate the nonlinearity, we separate phase and amplitude information. The phase misfit function is

$$\chi_\theta(m) = \frac{1}{2} \sum_{s=1}^S \sum_{r=1}^R \sum_{i=1}^N \omega_{rsi} \left\{ \frac{\Im [s_i^s(x_r, z_i; m) / d_i^s(x_r, z_i)]}{\Re [s_i^s(x_r, z_i; m) / d_i^s(x_r, z_i)]} \right\}^2, \quad (7)$$

and the amplitude misfit is

$$\chi_A(m) = \frac{1}{2} \sum_{s=1}^S \sum_{r=1}^R \sum_{i=1}^N \omega_{rsi} \log \left[ \left| \frac{s_i^s(x_r, z_i; m)}{d_i^s(x_r, z_i)} \right|^2 \right], \quad (8)$$

where the weight  $\omega_{rsi}$  for each source-station pair and component helps improve the convergence rate and is chosen to balance the contributions of short and long offsets. Although we can combine phase and amplitude information, here we only use the phase information. The phase information is stable and less affected by errors in the source location and magnitude in realistic data inversions.

**Postprocessing.** To improve the convergence rate and ill-posedness of FWI, we regularize the inversion in the model space. Therefore, we smooth the gradient of the misfit function by convolution with a 2D Gaussian gradient. The scale length is decided by the minimum length resolved by our simulations.

## Numerical experiments

We conduct different synthetic experiments to evaluate the added contribution of the horizontal components in SE-FWI. We compare models derived by two-component inversion with those that use only one component. In all experiments, density is assumed to be known. No pressure channels are being considered.

**Vertical-component inversion.** We analyze the resolution and sensitivity of using only the vertical component of the data to invert for elastic subsurface parameters. We conduct an elastic SE-FWI using the phase misfit  $\chi_\theta$  of equation 7. For all experiments, we perform the same number of iterations. For our multiscale strategy, in the first stage (S1), we use data in the frequency range of 2–5 Hz, increased by 0.06 Hz at each iteration. For the second stage (S2), we decrease the damping  $\gamma = 0.6$  s<sup>-1</sup> and increase the offset by the first-break time  $t_0^{st} \leq 4$  s. This stage assimilates later arrivals and also allows for larger scattering-angle perturbations. In the third stage (S3), the frequency band is broadened to 2–9 Hz, and the first-break times  $t_0^{st} \leq 5$  s. This bandwidth allows us to encode more sources in our simulation. Higher frequencies enable imaging smaller features. Finally, in the last stage (S4), we decrease  $\gamma = 0.3$  s<sup>-1</sup>, allowing for later reflections from deeper structures.

For analysis and quality control of the models reconstructed after the inversion, we use two different metrics: the relative model error,

$$\epsilon(m) = \frac{1}{N_m} \sum_{i=1}^N \frac{|m_i^R - m_i^T|}{m_i^T} \quad (9)$$

and the model correlation coefficient

$$R(m) = \frac{\sum_{i=1}^N (m_i^R - \bar{m}^R)(m_i^T - \bar{m}^T)}{\sqrt{\sum_{i=1}^N (m_i^R - \bar{m}^R)^2 \sum_{i=1}^N (m_i^T - \bar{m}^T)^2}}. \quad (10)$$

Here,  $m^R$  is the reconstructed model parameter,  $m^T$  is the target, and  $\bar{m}^R$  and  $\bar{m}^T$  is their respective means (for  $N_m$  the number of model mesh nodes). We compute both metrics for subregions within the model where the highest resolution is attained (dashed black square in Figure 4a). These are summarized in Figure 5.

In Figures 4b–4e, we show the models reconstructed ( $V_p$ ,  $V_s$ ) by using the vertical component of the data. The  $V_p$  model is

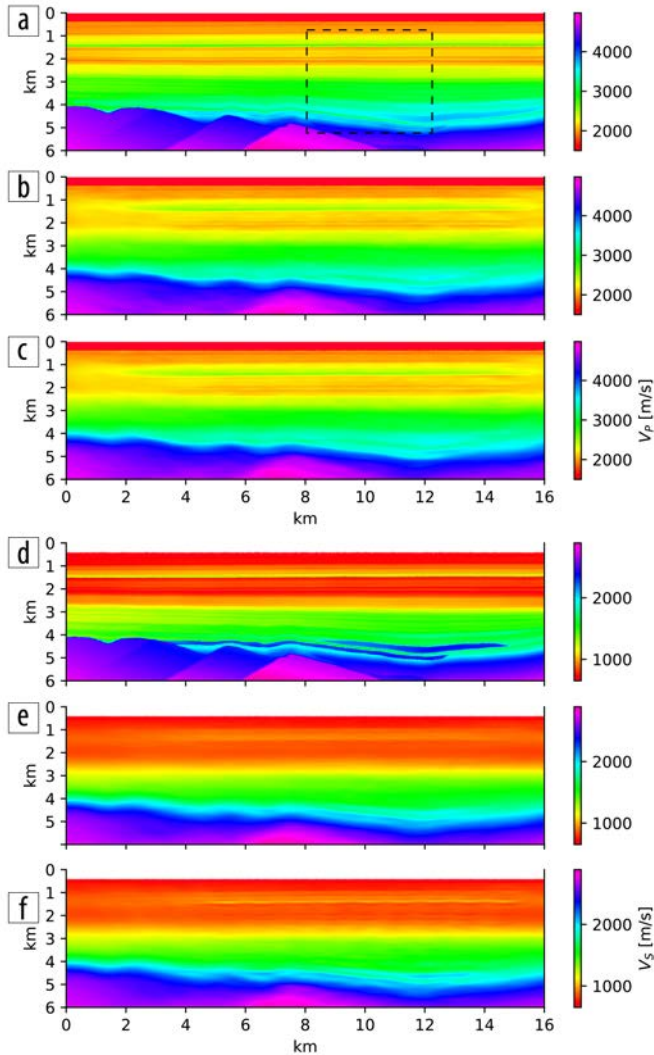


**Figure 4.** (a)  $V_p$  target model. (d)  $V_s$  target model. (b and e)  $V_p$  and  $V_s$  reconstructed models using the vertical components only. (c and f)  $V_p$  and  $V_s$  reconstructed models using both the vertical and horizontal components. Black dashed square depicts the region used to quantify the quality of the reconstructed models.

relatively well reconstructed at shallow depths (about 3 km), yet the model quality degrades with depth due to the spatial coverage. At 4–5 km depth, the model is only updated in the central part, recovering the high wave speed anomaly at this depth without reaching the correct magnitude and size. In the vertical profile shown in Figure 6a, the  $V_p$  reconstruction appears sharp down to about 4 km depth, after which the resolution decreases due to the maximum offset restriction in the data (13 km), which results in a mispositioned reflector (about 5 km depth). The shear wave speed ( $V_s$ ) target perturbations are underestimated. As shown in Figure 6a, the perturbations are well located (1.5 km, 4–5 km depth), but their amplitudes are smaller than in the target model.

**Vertical-and-horizontal-components inversion.** To analyze the resolution improvement achieved by incorporating the horizontal components into the inversion, we now perform elastic SE-FWI using both components of the data. We follow a similar inversion workflow as the vertical component inversion (phase misfit, multiscale approach, and same number of iterations). In the first stage (S1), we use a damping term  $\gamma = 1.1 \text{ s}^{-1}$ , the vertical component, and update only the compressional wave speed. Also, to avoid cycle

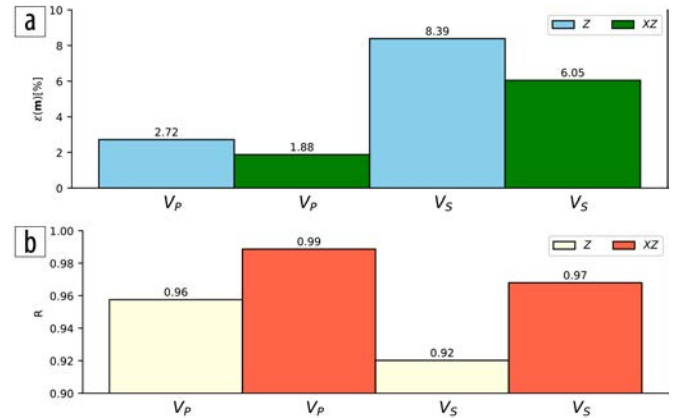


**Figure 5.** (a) Relative errors  $\epsilon(m)$  for models reconstructed using only the vertical (Z) or both horizontal and vertical (XZ). Smaller values mean better model reconstruction. (b) Correlation coefficients  $R$  for models reconstructed. Larger values signify better reconstruction.

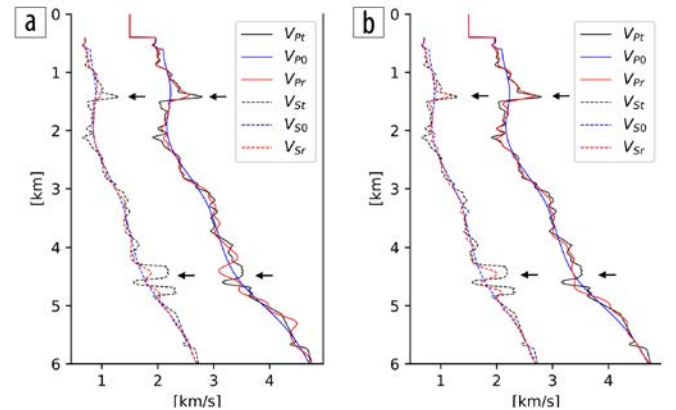


**Figure 6.** Vertical profiles at 10 km inline distance. (a) Target (black), initial (blue), and reconstructed (red) models of  $V_p$  (solid) and  $V_s$  (dashed) using vertical component inversion. (b) Target, initial, and reconstructed models using vertical and horizontal components. Arrows point to the principal model perturbations.

skipping, we restrict the offset with a maximum first-break time  $t_0^{si} \leq 3s$ . In stage 2 (S2), we add the horizontal component to the inversion to include P-to-S conversions. Additionally, we update both the compressional and the shear wave speed in the inversion ( $V_p$ ,  $V_s$ ), reduce the damping ( $\gamma = 0.6 \text{ s}^{-1}$ ) to include later arrivals, and increase the first-break time to  $t_0^{si} \leq 4s$ . For stage 3 (S3), we widen the bandwidth of the inversion from maximum frequency 5 to 9 Hz, and the break time to  $t_0^{si} \leq 5s$ . In the last stage (S4), we allow for later reflections from deeper structures.

## Discussion

By leveraging OBN seismic data acquisition technologies and the efficiency of source encoding for FWI, we investigate the improvement in resolution of ( $V_p$ ,  $V_s$ ) model reconstruction by incorporating horizontal components into our elastic SE-FWI workflow. The OBN's horizontal components are sensitive to P and P-to-S converted waves. S waves travel at a different speed than P waves. They sample different regions of the subsurface and provide additional information in terms of the elastic parameters (Ji et al., 2000; Bartana et al., 2024). We show that adding the horizontal component to the inversion improves the resolution for  $V_p$  and  $V_s$  models (Figures 4c–4f). Specifically, the  $V_p$  model perturbations at 4–5 km are better resolvable by the two-component inversion compared to the one-component inversion (Figure 4c). Additionally, the two-component inversion shows better quality compared to the one-component inversion, as evidenced by the relative percentage error  $\epsilon(\mathbf{m})$  and the correlation coefficient  $R(\mathbf{m})$  (Figures 5a and 5b). The oscillatory effect observed in the deepest (4–5 km)  $V_p$  anomaly in the vertical component inversion (Figure 6a) is being corrected by adding the horizontal component to the inversion (Figure 6b). In the case of the  $V_s$  model reconstruction, the vertical component inversion underestimates the magnitude of the anomalies. However, the main perturbations are well positioned at depth (about 4–5 km; Figure 6a). Conversely, while the two-component inversion underestimates the magnitude of model anomalies at both shallow and deep depths (Figures 4f and 6b), it provides a more accurate estimate compared to the one-component inversion.

## Conclusion

Compared to traditional vertical component SE-FWI, incorporating the horizontal components in SE-FWI has shown better and more robust results in the reconstruction of the elastic parameters of the subsurface. The improvement in model resolution highlights the importance of shear seismic waves, which are recorded mainly on the OBN horizontal components (Sears et al., 2008; Bartana et al., 2024). However, to exploit this new information, suitable inversion strategies have to be designed. The main objective of the inversion strategies is to gradually assimilate the information. Specially, with multicomponent OBN seismic acquisition, the data are dominated by P waves, resulting in greater sensitivity to compressional wave speed than shear wave speed (Sears et al., 2008). Therefore, as we showed in our experiments, inverting first for the  $V_p$  structure using the vertical component of the data, we can recover the long-wavelength perturbations by fixed  $V_s$  model, which acts as a second-order parameter in the inversion (Tarantola, 1984; Operto et al., 2013). Then, by

gradually increasing the offset, it is possible to recover deeper anomalies in the model. Additionally, because at wide aperture angles the data are also sensitive to the shear wave speed perturbations due to their diffraction radiation pattern, although to a lesser extent compared to  $V_p$  (Tarantola, 1984; Sears et al., 2008; Operto et al., 2013), we jointly update the  $V_s$  and  $V_p$  parameters in S2. In S3 and S4, P-to-S converted phases are inverted by adding the horizontal component of the data in the inversion. This new information improves the  $V_p$  and  $V_s$  models by adding small-scale features. The increase in quality demonstrates the P-to-S wave sensitivity to high-wavenumber features in the model parameters, specifically to  $V_s$ . Sears et al. (2008) have advocated for the use of horizontal components in ocean-bottom cable data to obtain  $V_p$  and  $V_s$  models. We have demonstrated the benefits of multicomponent OBN data in combination with source-encoded FWI and designed suitable inversion strategies for improving the resolution of reconstructed elastic parameters of the subsurface. The horizontal components of seismic data allow us to incorporate shear-wave information into FWI, resulting in a robust elastic model amenable to geologic interpretation. ■■■

## Acknowledgments

We thank the editors, Steven Brown, Ramesh Neelamani, and Partha Routh, and four anonymous reviewers, for their encouragement and constructive feedback. We also thank the Princeton Institute for Computational Science and Engineering (PICSciE) for its computational facilities and support.

## Data and materials availability

Data associated with this research are available and can be obtained by contacting the corresponding author.

Corresponding author: ae2415@princeton.edu

## References

- Bachmann, E., and J. Tromp, 2020, Source encoding for viscoacoustic ultrasound computed tomography: The Journal of the Acoustical Society of America, **147**, 3221–3235, <https://doi.org/10.1121/10.0001191>.
- Bartana, A., J. Codd, D. Kessler, J. Blanch, D. Eddy, R. Meza, V. Rambaran, J. Blangy, and Y. Huang, 2024, Full elastic imaging — Shenzi Field, deep-water Gulf of Mexico: First Break, **42**, no. 3, 55–63, <https://doi.org/10.3997/1365-2397.fb2024023>.
- Bunks, C., F. M. Saleck, S. Zaleski, and G. Chavent, 1995, Multiscale seismic waveform inversion: Geophysics, **60**, no. 5, 1457–1473, <https://doi.org/10.1190/1.1443880>.
- Castagna, J. P., M. L. Batzle, and R. L. Eastwood, 1985, Relationships between compressional-wave and shear-wave velocities in clastic silicate rocks: Geophysics, **50**, no. 4, 571–581, <https://doi.org/10.1190/1.1441933>.
- Cho, Y., C. Pérez Solano, J. Kimbro, Y. Yang, R.-É. Plessix, and K. Matson, 2022, Influence of shear velocity on elastic full-waveform inversion: Gulf of Mexico case study using multicomponent ocean-bottom node data: Geophysics, **87**, no. 5, R391–R400, <https://doi.org/10.1190/geo2022-0014.1>.
- Cui, C., E. Bachmann, D. Peter, Z. Liu, and J. Tromp, 2023, Source-encoded waveform inversion in the Northern Hemisphere: Geophysical Journal International, **235**, no. 3, 2305–2322, <https://doi.org/10.1093/gji/ggad363>.

- Gardner, G. H. F., L. W. Gardner, and A. R. Gregory, 1974, Formation velocity and density — The diagnostic basics for stratigraphic traps: *Geophysics*, **39**, no. 6, 770–780, <https://doi.org/10.1190/1.1440465>.
- Ji, Y., S. C. Singh, and B. E. Hornby, 2000 [2002], Sensitivity study using a genetic algorithm: Inversion of amplitude variations with slowness: *Geophysical Prospecting*, **48**, no. 6, 1053–1073, <https://doi.org/10.1046/j.1365-2478.2000.00226.x>.
- Krebs, J. R., J. E. Anderson, D. Hinkley, R. Neelamani, S. Lee, A. Baumstein, and M.-D. Lacasse, 2009, Fast full-wavefield seismic inversion using encoded sources: *Geophysics*, **74**, no. 6, WCC177–WCC188, <https://doi.org/10.1190/1.3230502>.
- Lailly, P., and J. Bednar, 1983, The seismic inverse problem as a sequence of before stack migrations: Proceedings of the Conference on Inverse Scattering — Theory and Application, 206–220.
- Liu, Z., J. Hoffmann, E. Bachmann, C. Cui, F. J. Simons, and J. Tromp, 2024, Laplace-domain crosstalk-free source-encoded elastic full-waveform inversion using time-domain solvers: *Geophysics*, **89**, no. 4, R355–R375, <https://doi.org/10.1190/geo2023-0351.1>.
- Operto, S., A. Miniussi, R. Brossier, L. Combe, L. Métivier, V. Monteiller, A. Ribodetti, and J. Virieux, 2015, Efficient 3-D frequency-domain mono-parameter full-waveform inversion of ocean-bottom cable data: Application to Valhall in the visco-acoustic vertical transverse isotropic approximation: *Geophysical Journal International*, **202**, no. 2, 1362–1391, <https://doi.org/10.1093/gji/ggv226>.
- Operto, S., Y. Gholami, V. Prieux, A. Ribodetti, R. Brossier, L. Métivier, and J. Virieux, 2013, A guided tour of multiparameter full-waveform inversion with multicomponent data: From theory to practice: *The Leading Edge*, **32**, no. 9, 1040–1054, <https://doi.org/10.1190/tle32091040.1>.
- Plessix, R.-E., 2006, A review of the adjoint-state method for computing the gradient of a functional with geophysical applications: *Geophysical Journal International*, **167**, no. 2, 495–503, <https://doi.org/10.1111/j.1365-246X.2006.02978.x>.
- Pratt, R. G., 1999, Seismic waveform inversion in the frequency domain, Part 1: Theory and verification in a physical scale model: *Geophysics*, **64**, no. 3, 888–901, <https://doi.org/10.1190/1.1444597>.
- Romero, L. A., D. C. Ghiglia, C. C. Ober, and S. A. Morton, 2000, Phase encoding of shot records in prestack migration: *Geophysics*, **65**, no. 2, 426–436, <https://doi.org/10.1190/1.1444737>.
- Schuster, G. T., X. Wang, Y. Huang, W. Dai, and C. Boonyasirawat, 2011, Theory of multisource crosstalk reduction by phase-encoded statics: *Geophysical Journal International*, **184**, no. 3, 1289–1303, <https://doi.org/10.1111/j.1365-246X.2010.04906.x>.
- Sears, T. J., S. C. Singh, and P. J. Barton, 2008, Elastic full waveform inversion of multi-component OBC seismic data: *Geophysical Prospecting*, **56**, no. 6, 843–862, <https://doi.org/10.1111/j.1365-2478.2008.00692.x>.
- Shin, C., and Y. H. Cha, 2009, Waveform inversion in the Laplace–Fourier domain: *Geophysical Journal International*, **177**, no. 3, 1067–1079, <https://doi.org/10.1111/j.1365-246X.2009.04102.x>.
- Solano, C. P., and R.-É. Plessix, 2023, Can elastic waveform inversion benefit from inverting multicomponent data?: *The Leading Edge*, **42**, no. 3, 184–189, <https://doi.org/10.1190/tle42030184.1>.
- Tarantola, A., 1984, Linearized inversion of seismic reflection data: *Geophysical Prospecting*, **32**, no. 6, 998–1015, <https://doi.org/10.1111/j.1365-2478.1984.tb00751.x>.
- Tromp, J., and E. Bachmann, 2019, Source encoding for adjoint tomography: *Geophysical Journal International*, **218**, no. 3, 2019–2044, <https://doi.org/10.1093/gji/ggz271>.
- Tromp, J., C. Tape, and Q. Liu, 2005, Seismic tomography, adjoint methods, time reversal and banana-doughnut kernels: *Geophysical Journal International*, **160**, no. 1, 195–216, <https://doi.org/10.1111/j.1365-246X.2004.02453.x>.
- Zhang, D., C. Tsingas, A. A. Ghamdi, M. Huang, W. Jeong, K. K. Sliz, S. M. Aldeghaither, and S. A. Zahrani, 2021, A review of OBN processing: Challenges and solutions: *Journal of Geophysics and Engineering*, **18**, no. 4, 492–502, <https://doi.org/10.1093/jge/gxab024>.
- Zhang, Q., W. Mao, H. Zhou, H. Zhang, and Y. Chen, 2018, Hybrid-domain simultaneous-source full waveform inversion without crosstalk noise: *Geophysical Journal International*, **215**, no. 3, 1659–1681, <https://doi.org/10.1093/gji/ggy366>.